MITSUBISHI ELECTRIC RESEARCH LABORATORIES
https://www.merl.com

Optimal Measurement Projection in GNSS-RTK Factor Graph Optimization

Hu, Yingjie; Di Cairano, Stefano; Berntorp, Karl

TR2025-118 August 20, 2025

Abstract

This paper presents two optimal measurement projection schemes for the factor-graph-based Global Navi- gation Satellite System (GNSS) positioning with Real-Time- Kinematics (RTK). While factor graph optimization (FGO) has demonstrated improved accuracy and robustness in GNSS positioning compared to conventional filtering-based methods, the improvement has a cost of increased computational com- plexity due to the fact that FGO processes the batch of historical data simultaneously. Two measurement projection schemes are proposed to alleviate the computational burden of FGO by optimally projecting the GNSS measurements into a lower-dimensional subspace. Thereby, the dimensionality of the factor graph optimization is significantly reduced with only minimally performance loss. Monte Carlo simulation results demonstrate that the proposed measurement reduction schemes can achieve a significant computational speedup for the FGO- based GNSS-RTK positioning while retaining high-precision positioning performance.

IEEE Conference on Control Technology and Applications (CCTA) 2025

Mitsubishi Electric Research Laboratories, Inc.
201 Broadway, Cambridge, Massachusetts 02139

Optimal Measurement Projection in GNSS-RTK Factor Graph Optimization

Yingjie Hu, Stefano Di Cairano*, Karl Berntorp

***Abstract*— This paper presents two optimal measurement projection schemes for the factor-graph-based Global Navigation Satellite System (GNSS) positioning with Real-Time-Kinematics (RTK). While factor graph optimization (FGO) has demonstrated improved accuracy and robustness in GNSS positioning compared to conventional filtering-based methods, the improvement has a cost of increased computational complexity due to the fact that FGO processes the batch of historical data simultaneously. Two measurement projection schemes are proposed to alleviate the computational burden of FGO by optimally projecting the GNSS measurements into a lower-dimensional subspace. Thereby, the dimensionality of the factor graph optimization is significantly reduced with only minimally performance loss. Monte Carlo simulation results demonstrate that the proposed measurement reduction schemes can achieve a significant computational speedup for the FGO-based GNSS-RTK positioning while retaining high-precision positioning performance.**

I. Introduction

High-precision positioning is vital for many positioning, navigation, and timing (PNT) applications, including autonomous vehicles, unmanned aerial vehicles (UAVs), and aircraft. GNSS-RTK is widely used to achieve such accuracy by leveraging pseudorange (code) and carrier phase measurements. Pseudorange offers meter-level accuracy, affected by atmospheric delays, clock biases, and multipath effects. In contrast, carrier phase measurements provide sub-centimeter accuracy but suffer from integer ambiguities due to the unknown number of full carrier wave cycles during signal transit. Resolving integer ambiguities is key to GNSS-RTK positioning, but this process can be computationally complex and sensitive to cycle slips, which are sudden jumps of the integer ambiguities caused by the loss-of-lock of the carrier signal tracking.

Prior work: Traditional ambiguity resolution follows a two-step process: float ambiguities are first estimated, then constrained to integer values (e.g., using LAMBDA method [12]). After resolving integer ambiguities, receiver states are updated using these integer estimates, enabling high-precision positioning solutions. Filtering-based methods estimate the GNSS receiver states epoch-by-epoch. Alternatively, Factor Graph Optimization (FGO), a nonlinear optimization framework, estimates the state trajectory by processing the batch of historical epoch data simultaneously. FGO exploits the full data batch, capturing temporal correlations between measurements and states to produce globally consistent estimates [14]. FGO's iterative optimization enables it to handle nonlinearity more effectively over extended Kalman filter (EKF) [15], and recent studies have adopted FGO for GNSS-RTK positioning [11], [14].

Challenge: FGO's batch optimization leads to high computational cost, especially for large datasets. To address this, algorithms like iSAM [8] and iSAM2 [7] are proposed to improve the computational efficiency via incremental updates. For long-duration tasks, sliding-window approaches [15] can further reduce the computational burden by processing only the data within the current sliding window at each time. The window size represents a trade-off between performance and computational load: a smaller window reduces computational burden but limits the amount of data available for graph optimization, potentially reducing FGO's performance.

Contribution: This paper proposes two optimal measurement projection algorithms for FGO-based GNSS-RTK positioning with sliding window implementation. The goal is to reduce FGO's computational load while preserving high precision positioning performance. In GNSS positioning, optimal estimators are designed to minimize the mean square error (MSE) of the state estimates, with the best achievable performance defined by the Cramer-Rao Lower Bound (CRLB) [9]. Consequently, our measurement projection algorithms aim to find the optimal linear projection operator that minimizes the MSE of the state estimates when using the projected measurements of reduced dimensions. On one hand, the optimal projection ensures that the CRLB is only minimally affected by the use of the projected measurements, leading to nearly identical positioning performance between the original and the projected measurements. On the other hand, the reduced dimensionality of the projected measurements decreases the computational complexity of the FGO. Monte Carlo simulations validate the proposed methods, showing significant computational savings with minimal accuracy loss.

II. Problem Setup

To simplify the exposition, we assume GNSS code and carrier phase measurements and ignore Doppler measurements. Consider the following code and carrier phase measurement models from satellite s to receiver r at time t_k,

$$\begin{aligned}\rho^s_{r,k} &= r^s_{r,k} + c(\delta t_{r,k} - \delta t^s_k) + I^s_{r,k} + T^s_{r,k} + \epsilon^s_{r,k}\\ \lambda\phi^s_{r,k} &= r^s_{r,k} + c(\delta t_{r,k} - \delta t^s_k) - I^s_{r,k} + T^s_{r,k} + \lambda N^s_{r,k} + \eta^s_{r,k}\end{aligned} \tag{1}$$

where $\rho^s_{r,k}$ is the code measurement, $\phi^s_{r,k}$ is the carrier phase measurement, and $r^s_{r,k} = \|\mathbf{p}_{r,k} - \mathbf{p}_{s,k}\|$ is the geometric range between receiver r and satellite s. $\mathbf{p}_{r,k}, \mathbf{p}_{s,k} \in \mathbb{R}^3$

Yingjie Hu (hu000258@umn.edu) is with the Department of Aerospace Engineering and Mechanics at the University of Minnesota, Twin Cities. Stefano Di Cairano (dicairano@merl.com) and Karl Berntorp (karl.o.berntorp@ieee.org) are with Mitsubishi Electric Research Labs (MERL), Cambridge, MA, USA.

denote the receiver and satellite positions, c is the speed of light, $\delta t_{r,k}$ is the receiver clock bias, and δt^s_k is the satellite clock bias. $I^s_{r,k}$ denotes the ionospheric delay, $T^s_{r,k}$ is the tropospheric delay, and λ represents the carrier wavelength. Furthermore, $N^s_{r,k}$ represents the carrier phase integer ambiguity, and $\epsilon^s_{r,k}$ and $\eta^s_{r,k}$ denote the measurement errors, generally caused by multipath effects, NLOS receptions, receiver noise, and antenna delay [14]. $\epsilon^s_{r,k}$ and $\eta^s_{r,k}$ are assumed to be white Gaussian noises, the variance of which depends on the satellite elevation.

A single differencing (SD) operation is typically performed between the measurements of receiver r and base b to eliminate common-mode errors (e.g., ionosphere, troposphere, and satellite clock) within a local vicinity [5],

$$\begin{aligned}\Delta\rho^s_{br,k} &= r^s_{b,k} - r^s_{r,k} + c(\delta t^s_{b,k} - \delta t^s_{r,k}) + \Delta\epsilon^s_{br,k}\\ \lambda\Delta\phi^s_{br,k} &= r^s_{b,k} - r^s_{r,k} + c(\delta t^s_{b,k} - \delta t^s_{r,k}) + \lambda\Delta N^s_{br,k} + \Delta\eta^s_{br,k}\end{aligned} \tag{2}$$

Next, a second difference is performed between the reference (pivot) satellite o and satellite s to remove the receiver clock bias [2]. The resulting double-differenced (DD) code and carrier phase measurements can be expressed as

$$\begin{aligned}\nabla\Delta\rho^{so}_{br,k} &= \nabla\Delta r^{so}_{br,k} + \nabla\Delta\epsilon^{so}_{br,k}\\ \lambda\nabla\Delta\phi^{so}_{br,k} &= \nabla\Delta r^{so}_{br,k} + \lambda\nabla\Delta N^{so}_{br,k} + \nabla\Delta\eta^{so}_{br,k}\end{aligned} \tag{3}$$

where $\nabla\Delta r^{so}_{br,k} = (r^s_{b,k} - r^s_{r,k}) - (r^o_{b,k} - r^o_{r,k})$, and $\nabla\Delta N^{so}_{br,k} = \Delta N^s_{br,k} - \Delta N^o_{br,k}$ is the DD ambiguity. If M pairs of DD code and carrier phase measurements are available at time t_k (M+1 satellites $o, s_1, s_2, \cdots, s_M$ are visible), we can form the DD code and carrier phase measurement equations

$$\begin{aligned}\mathbf{y}_{\rho,k} &= \mathbf{h}(\mathbf{x}_k) + \boldsymbol{\epsilon}_k\\ \mathbf{y}_{\phi,k} &= \mathbf{h}(\mathbf{x}_k) + \lambda\mathbf{n}_k + \boldsymbol{\eta}_k\end{aligned} \tag{4}$$

where the receiver state $\mathbf{x}_k$ includes at least the receiver's position and velocity $\mathbf{x}_k = \begin{bmatrix}\mathbf{p}^\top_{r,k} & \mathbf{v}^\top_{r,k}\end{bmatrix}^\top$, $\mathbf{n}_k \in \mathbb{Z}^M$ is the DD carrier phase integer ambiguity vector, $\boldsymbol{\epsilon}_k \sim \mathcal{N}(\boldsymbol{\epsilon}_k|\mathbf{0}, \mathbf{R}_{\rho,k})$ and $\boldsymbol{\eta}_k \sim \mathcal{N}(\boldsymbol{\eta}_k|\mathbf{0}, \mathbf{R}_{\phi,k})$, and

$$\begin{aligned}\mathbf{h}(\mathbf{x}_k) &= \begin{bmatrix}\nabla\Delta r^{s_1o}_{br,k} & \cdots & \nabla\Delta r^{s_Mo}_{br,k}\end{bmatrix}^T\\ \mathbf{n}_k &= \begin{bmatrix}\nabla\Delta N^{s_1o}_{br,k} & \cdots & \nabla\Delta N^{s_Mo}_{br,k}\end{bmatrix}^T\\ \boldsymbol{\epsilon}_k &= \begin{bmatrix}\nabla\Delta\epsilon^{s_1o}_{br,k} & \cdots & \nabla\Delta\epsilon^{s_Mo}_{br,k}\end{bmatrix}^T\\ \boldsymbol{\eta}_k &= \begin{bmatrix}\nabla\Delta\eta^{s_1o}_{br,k} & \cdots & \nabla\Delta\eta^{s_Mo}_{br,k}\end{bmatrix}^T.\end{aligned} \tag{5}$$

In this work, we use the constant-velocity (CV) model [4] as follows to characterize the receiver motion.

$$\mathbf{x}_{k+1} = \begin{bmatrix}\mathbf{I} & dt\mathbf{I}\\ \mathbf{0} & \mathbf{I}\end{bmatrix}\mathbf{x}_k + \begin{bmatrix}\frac{dt^2}{2}\mathbf{I}\\ dt\mathbf{I}\end{bmatrix}\mathbf{w}_k \tag{6}$$

where dt is the sampling period and $\mathbf{w}_k$ is the Gaussian process noise $\mathbf{w}_k \sim \mathcal{N}(\mathbf{w}_k|\mathbf{0}, \mathbf{Q}_k)$. Note that our proposed methodology is not limited to linear motion models and more sophisticated models can be used for the receiver dynamics.

III. The Baseline GNSS-RTK FGO

In this section, we briefly outline the GNSS-RTK FGO algortihm presented in [6], which we will augment with the optimal measurement projections in later sections. For more details on the original algorithm, please refer to [6].

The baseline algorithm, illustrated in Fig. 1, consists of two FGOs. It is implemented using a sliding window. Current sliding window spans through time step $k+1$ to $k+T$. The first-stage FGO computes the float solution of receiver states $\hat{\mathbf{x}}_{1:\text{T,float}}$ and ambiguities $\hat{\mathbf{n}}_{1:\text{T,float}}$ within the current sliding window. The subscript 1:T denotes indices within the window. Next, LAMBDA method is used to obtain the integer ambiguity estimates $\hat{\mathbf{n}}_{1:\text{T,fix}}$. Subsequently, the second-stage FGO computes the fixed solution of the receiver states $\hat{\mathbf{x}}_{1:\text{T,fix}}$. $\hat{\mathbf{x}}_{\text{T,fix}}$ is output as the receiver state estimate of time step $k+T$. Then the sliding window moves forward by one step and repeats this process, using the previous solution as prior information. The components of the baseline FGO algorithm is discussed as follows:

1) DD carrier phase factor: Based on (4), for the first-stage FGO, DD carrier phase factor can be expressed as

$$\|e^{\text{I}}_{\phi,i}\|^2_{\mathbf{R}_{\phi,i}} = \|\mathbf{y}_{\phi,i} - \mathbf{h}(\mathbf{x}_i) - \lambda\mathbf{n}_i\|^2_{\mathbf{R}_{\phi,i}} \tag{7}$$

where the superscript I represents the first FGO and subscript i denotes the index within the sliding window. The DD carrier phase factor of the second-stage FGO is

$$\|e^{\text{II}}_{\phi,i}\|^2_{\mathbf{R}_{\phi,i}} = \|\mathbf{y}_{\phi,i} - \mathbf{h}(\mathbf{x}_i) - \lambda\hat{\mathbf{n}}_{i,\text{fix}}\|^2_{\mathbf{R}_{\phi,i}}. \tag{8}$$

2) DD pseudorange factor: DD pseudorange (code) measurements only depend on receiver states. Thus, the error factor of DD pseudorange is the same for both the first and second FGO,

$$\|e_{\rho,i}\|^2_{\mathbf{R}_{\rho,i}} = \|\mathbf{y}_{\rho,i} - \mathbf{h}(\mathbf{x}_i)\|^2_{\mathbf{R}_{\rho,i}}. \tag{9}$$

3) Motion constraint factor: motion constraints on receiver states between consecutive time steps can be derived from (6). Denote the equivalent process noise covariance matrix by $\bar{\mathbf{Q}}_i = \mathbf{B}_i\mathbf{Q}_i\mathbf{B}^\top_i$. Thus, the motion constraint factor is

$$\|e_{x,i}\|^2_{\bar{\mathbf{Q}}_i} = \|\mathbf{x}_{i+1} - \mathbf{F}_i\mathbf{x}_i\|^2_{\bar{\mathbf{Q}}_i}. \tag{10}$$

4) Adaptive ambiguity factor: The time evolution of the ambiguity vector $\mathbf{n}_i$ is modeled as an adaptive random walk by adapting the random walk noise to reflect the integer discontinuity caused by cycle slips. It enables FGO to leverage the time correlation in the integer ambiguity evolution and enhances the robustness to cycle slips.

$$\|e_{n,i}\|^2_{\mathbf{V}_i} = \|\mathbf{n}_{i+1} - \mathbf{n}_i\|^2_{\mathbf{V}_i}. \tag{11}$$

where $\mathbf{V}_i$ is the covariance of the adaptive ambiguity noise. When a cycle slip is detected for a certain ambiguity variable, the corresponding variance in $\mathbf{V}_i$ is inflated to reflect the integer jump. When there is no cycle slip, the corresponding variance remains a small value. A detailed derivation of $\mathbf{V}_i$ can be found in Sec.III in [6].

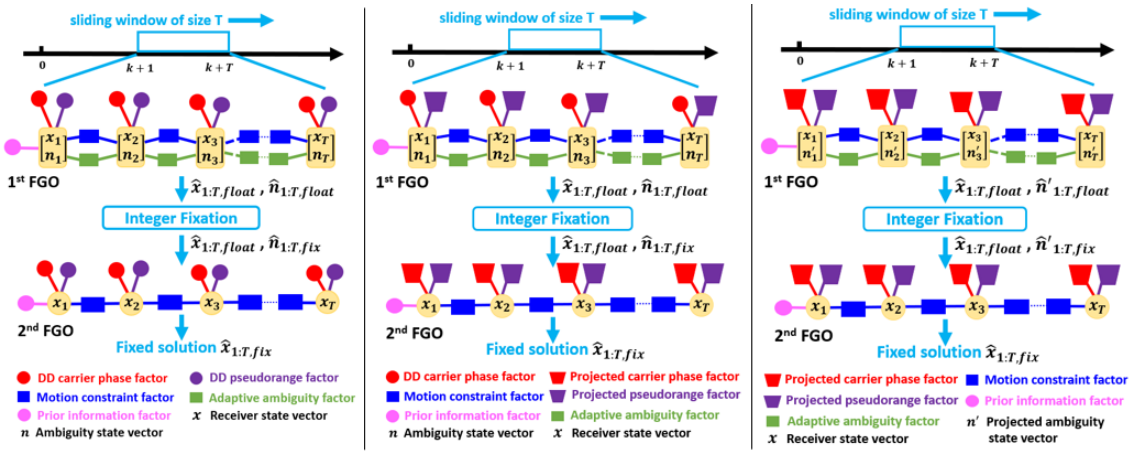

Fig. 1. Architecture of the baseline FGO-based GNSS-RTK algorithm (left), measurement projection scheme I (middle), measurement projection scheme II (right). The subscript $1:T$ denotes the indices within the sliding window.

5) Prior information factor: In sliding-window FGO, a prior information factor incorporates historical data from the previous window to the current one. Specifically, the fixed state estimates at the second time step of the previous window is used as the prior for the current window, denoted as $\begin{bmatrix}\hat{\mathbf{x}}_{\text{pri}}^T & \hat{\mathbf{n}}_{\text{pri}}^T\end{bmatrix}^T$ with associated covariance matrix $\mathbf{P}_{\text{pri}}$. The state vector at the first time step of the current window is $\begin{bmatrix}\mathbf{x}_1^T & \mathbf{n}_1^T\end{bmatrix}^T$. The prior information factor of the first-stage FGO is expressed as

$$\|e_{\text{pri}}^{\text{I}}\|_{\mathbf{P}_{\text{pri}}}^2 = \| \begin{bmatrix}\mathbf{x}_1^T & \mathbf{n}_1^T\end{bmatrix}^T - \begin{bmatrix}\hat{\mathbf{x}}_{\text{pri}}^T & \hat{\mathbf{n}}_{\text{pri}}^T\end{bmatrix}^T \|_{\mathbf{P}_{\text{pri}}}^2. \tag{12}$$

Solving the first-stage FGO yields float solutions $\hat{\mathbf{x}}_{1:\text{T, float}}$ and $\hat{\mathbf{n}}_{1:\text{T, float}}$. Then, $\hat{\mathbf{x}}_{1,\text{ float}}$, the receiver state estimate at the first time step of current sliding window, will be utilized as the prior information for the second-stage FGO. The prior information factor of the second-stage FGO is

$$\|e_{\text{pri}}^{\text{II}}\|_{\mathbf{P}_{1,\text{float}}}^2 = \|\mathbf{x}_1 - \hat{\mathbf{x}}_{1,\text{ float}}\|_{\mathbf{P}_{1,\text{float}}}^2. \tag{13}$$

FGO can be solved using iterative methods (e.g. Gauss-Newton, Levenberg-Marquardt). However, this process can become computationally intensive, particularly when the number of GNSS measurements is large and the sliding window size is substantial.

IV. Optimal Measurement Projection

we use a concrete example here to illustrate FGO's computational burden. Receiver state $\mathbf{x} \in \mathbb{R}^6$, integer ambiguity vector $\mathbf{n} \in \mathbb{Z}^M$, and sliding window size T. The first-stage FGO has a dimensionality of $(6+M)\times T$, as shown in Fig. 1, which scales with M and T. For instance, with 13 visible satellites ($M = 12$) and sliding window size $T = 60$, the FGO's dimensionality is 1080. While larger M improves positioning accuracy, it significantly increases computational cost. Conversely, reducing T to mitigate this burden can potentially degrade FGO performance. To address this issue, we propose projecting GNSS measurements into a lower-dimensional subspace of size $\tilde{M}$ ($\tilde{M} < M$), reducing the computational complexity while minimally impacting GNSS-RTK FGO positioning performance.

A. Measurement Projection Formulation

Considering the measurement model: $\mathbf{y}_k = \mathbf{h}(\mathbf{x}_k) + \boldsymbol{v}_k$ where $\mathbf{y}_k \in \mathbb{R}^M$, and $\boldsymbol{v}_k \sim \mathcal{N}(\mathbf{0}, \mathbf{R}_k)$. We seek an optimal linear projector $\boldsymbol{\Psi}_k \in \mathbb{R}^{\tilde{M}\times M}$ such that $\tilde{\mathbf{y}}_k = \boldsymbol{\Psi}_k \mathbf{y}_k \in \mathbb{R}^{\tilde{M}}$ ($\tilde{M} < M$) while retaining maximal information from the original measurement sets [3]. The subscript k is dropped for brevity. The optimality criterion of the measurement projection is selected to be the minimization of the MSE of the state estimate $\hat{\mathbf{x}}$ using projected measurements $\tilde{\mathbf{y}}$. The CRLB states that for any unbiased estimate $\hat{\mathbf{x}}$ [9],

$$\mathbb{E}[(\mathbf{x}-\hat{\mathbf{x}})(\mathbf{x}-\hat{\mathbf{x}})^\top] \geq \boldsymbol{\mathcal{I}}(\mathbf{x})^{-1} \tag{14a}$$

$$\boldsymbol{\mathcal{I}}(\mathbf{x}) = (\boldsymbol{\Psi}\mathbf{H})^\top(\boldsymbol{\Psi}\mathbf{R}\boldsymbol{\Psi}^\top)^{-1}(\boldsymbol{\Psi}\mathbf{H}) \tag{14b}$$

where $\boldsymbol{\mathcal{I}}(\mathbf{x})$ denotes the Fisher Information Matrix (FIM) of $\mathbf{x}$, measuring the amount of information contained in the measurements, and $\mathbf{H} = (\partial \mathbf{h}(\mathbf{x}))/(\partial \mathbf{x})|_{\mathbf{x}=\hat{\mathbf{x}}}$. (14a) provides the theoretical lower bound on the variance of any unbiased estimate $\hat{\mathbf{x}}$ of $\mathbf{x}$. Consequently, the optimization program of minimizing the state estimate MSE can be formulated as

$$\begin{aligned}\boldsymbol{\Psi}^* &= \underset{\boldsymbol{\Psi}}{\operatorname{argmin}}\, J(\boldsymbol{\Psi}) = \underset{\boldsymbol{\Psi}}{\operatorname{argmin}}\, \operatorname{Tr}\left(\boldsymbol{\mathcal{I}}^{-1}(\mathbf{x})\right) \\ &= \underset{\boldsymbol{\Psi}}{\operatorname{argmin}}\, \operatorname{Tr}\left(\{(\boldsymbol{\Psi}\mathbf{H})^\top(\boldsymbol{\Psi}\mathbf{R}\boldsymbol{\Psi}^\top)^{-1}(\boldsymbol{\Psi}\mathbf{H})\}^{-1}\right)\end{aligned} \tag{15}$$

For $\boldsymbol{\Psi} = \boldsymbol{I} \in \mathbb{R}^{M\times M}$, $J(\boldsymbol{I})$ represents the smallest achievable MSE of state estimates using the original measurement sets. $J(\boldsymbol{\Psi}) \geq J(\boldsymbol{I}), \forall \boldsymbol{\Psi} \in \mathbb{R}^{\tilde{M}\times M}$ and $\tilde{M} \leq M$ as the linear combination of measurements do not contribute new information.

B. Solving the Optimization Program

A gradient-descent-based method is proposed in [3] to solve the nonconvex optimization (15). The partial derivative of $J(\boldsymbol{\Psi})$ with respect to $\boldsymbol{\Psi}$ can be computed by

$$\partial J(\boldsymbol{\Psi})/\partial \boldsymbol{\Psi} = -2\boldsymbol{U}\boldsymbol{Q}\boldsymbol{\Lambda}^{-2}\boldsymbol{Q}^\top\boldsymbol{V}^\top \tag{16}$$

$$\begin{aligned}\boldsymbol{Y} &= \mathbf{H}^\top\boldsymbol{\Psi}^\top(\boldsymbol{\Psi}\mathbf{R}\boldsymbol{\Psi}^\top)^{-1}\boldsymbol{\Psi}\mathbf{H} = \boldsymbol{Q}\boldsymbol{\Lambda}\boldsymbol{Q}^\top \\ \boldsymbol{U} &= (\boldsymbol{\Psi}\mathbf{R}\boldsymbol{\Psi}^\top)^{-1}\boldsymbol{\Psi}\mathbf{H}, \quad \boldsymbol{V} = \mathbf{H} - \mathbf{R}\boldsymbol{\Psi}^\top\boldsymbol{U}\end{aligned} \tag{17}$$

Thus, a simple gradient-descent algorithm using (16) can be developed to compute a local optimum of the measurement projection optimization in (15). Let superscript $[s]$ denote the gradient-descent iteration index. At $s=0$, $\boldsymbol{\Psi}_{[0]} \in \mathbb{R}^{\tilde{M}\times M}$ is randomly initialized, e.g., via uniform distribution $\mathcal{U}(-1,1)$. Each gradient-descent iteration updates the $\boldsymbol{\Psi}_{[s]}$ as follows.

$$\begin{aligned}
\boldsymbol{\Psi}_{[s+1]} &= \boldsymbol{\Psi}_{[s]} + 2\gamma \boldsymbol{U}_{[s]}\boldsymbol{Q}_{[s]}\boldsymbol{\Lambda}_{[s]}^{-2}\boldsymbol{Q}_{[s]}^{\top}\boldsymbol{V}_{[s]}^{\top} \\
\Big[\boldsymbol{\Lambda}_{[s]}, \boldsymbol{Q}_{[s]}\Big] &= \mathrm{eig}(\boldsymbol{Y}_{[s]}), \quad \boldsymbol{Y}_{[s]} = \mathbf{H}^{\top}\boldsymbol{\Psi}_{[s]}^{\top}\boldsymbol{U}_{[s]} \\
\boldsymbol{V}_{[s]} &= \mathbf{H} - \mathbf{R}\boldsymbol{\Psi}_{[s]}^{\top}\boldsymbol{U}_{[s]}, \quad \boldsymbol{U}_{[s]} = (\boldsymbol{\Psi}_{[s]}\mathbf{R}\boldsymbol{\Psi}_{[s]}^{\top})^{-1}\boldsymbol{\Psi}_{[s]}\mathbf{H} \\
\boldsymbol{H} &= \partial \mathbf{h}(\mathbf{x})/\partial \mathbf{x}|_{\mathbf{x}=\hat{\mathbf{x}}}
\end{aligned} \tag{18}$$

Equation (18) ensures that $\boldsymbol{\Psi}_{[s]}$ converges to a local optimum for a large s if the step size γ is found by a line-search. $\boldsymbol{\Psi}^*$ denotes the computed optimal projector. Next, we introduce the two design schemes of applying this optimal measurement projection approach to the baseline GNSS-RTK FGO.

V. Measurement Projection Scheme I

Fig. 1 shows the diagram of the baseline GNSS-RTK FGO. Within the sliding window of size T, pseudorange and carrier phase measurements $\mathbf{y}_{\rho,i},\ \mathbf{y}_{\phi,i} \in \mathbb{R}^{M},\ i=1,\cdots,T$. According to (4), $\mathbf{y}_{\rho,i}$ only contains the receiver states $\mathbf{x}_i$ while $\mathbf{y}_{\phi,i}$ contains both $\mathbf{x}_i$ and integer ambiguity $\mathbf{n}_i$. In projection scheme I, the optimality criterion is minimize the MSE of the positional state estimate $\hat{\mathbf{p}}$. As shown in Fig. 1, in the first-stage FGO, pseduorange measurements $\{\mathbf{y}_{\rho,i}\}_{i=1}^{T}$ are projected from $\mathbb{R}^{M}$ to $\mathbb{R}^{\tilde{M}}$ and $\tilde{M} < M$. Carrier phase measurements $\{\mathbf{y}_{\phi,i}\}_{i=1}^{T}$ remain the same because the estimation of the integer ambiguity will become unobservable if $\{\mathbf{y}_{\phi,i}\}_{i=1}^{T}$ are projected to a lower-dimensional subspace. For the second-stage FGO, integer ambiguities are resolved. $\{\mathbf{y}_{\phi,i}\}_{i=1}^{T}$ free of the integer ambiguities can then be projected from from $\mathbb{R}^{M}$ to $\mathbb{R}^{\tilde{M}}$.

Given (4) and (5), $\mathbf{y}_{\rho,i} = \mathbf{h}(\mathbf{x}_i) + \boldsymbol{\epsilon}_i = \mathbf{h}(\mathbf{p}_i) + \boldsymbol{\epsilon}_i$ as the geometric range $\mathbf{h}(\mathbf{x}_i)$ does not depend on the receiver velocity. Thus, the Jacobian of $\mathbf{h}(\mathbf{p}_i)$ with respect to the position states $\mathbf{p}_i$ is

$$\mathbf{H}_{\mathbf{p}_i} = \left(\partial \mathbf{h}(\mathbf{p}_i)\right) / \left(\partial \mathbf{p}_i\right)|_{\mathbf{p}_i=\hat{\mathbf{p}}_i} \tag{19}$$

where, $\hat{\mathbf{p}}_i$ is the current position estimate. According to (15), the optimal measurement projection optimization for $\mathbf{y}_{\rho,i}$ can be expressed as

$$\boldsymbol{\Psi}_{\rho,i}^{*} = \underset{\boldsymbol{\Psi}_i}{\mathrm{argmin}}\, \mathrm{Tr}\left(\{(\boldsymbol{\Psi}_i\mathbf{H}_{\mathbf{p}_i})^{\top}(\boldsymbol{\Psi}_i\mathbf{R}_{\rho,i}\boldsymbol{\Psi}_i^{\top})^{-1}(\boldsymbol{\Psi}_i\mathbf{H}_{\mathbf{p}_i})\}^{-1}\right) \tag{20}$$

Since the receiver's position change within the sliding window is minimal compared to the satellite-receiver distance, the variation in the Jacobian matrix $\mathbf{H}_{\mathbf{p}_i}$ over time within the sliding window is expected to be negligible, which suggests that $\mathbf{H}_{\mathbf{p}_i}$ can be treated as nearly constant within the sliding window without significant loss of accuracy. Given that the noise covariance $\mathbf{R}_{\rho,i}$ is assumed known and constant, $\boldsymbol{\Psi}_{\rho,1}^{*}$ computed at the first time step within the sliding window can be used to project $\{\mathbf{y}_{\rho,i}\}_{i=1}^{T}$ for the entire window. The error factor of the projected pseudorange is expressed by

$$\|\tilde{e}_{\rho,i}\|_{\tilde{\mathbf{R}}_{\rho,i}}^{2} = \|\boldsymbol{\Psi}_{\rho,1}^{*}\mathbf{y}_{\rho,i} - \boldsymbol{\Psi}_{\rho,1}^{*}\mathbf{h}(\mathbf{x}_i)\|_{\tilde{\mathbf{R}}_{\rho,i}}^{2} \tag{21}$$

where $\tilde{\mathbf{R}}_{\rho,i} = \boldsymbol{\Psi}_{\rho,1}^{*}\mathbf{R}_{\rho,i}\boldsymbol{\Psi}_{\rho,1}^{*\top}$. After the integer ambiguity resolution, the ambiguity vectors $\hat{\mathbf{n}}_{1:\mathrm{T,fix}}$ can be removed from the carrier phase measurements $\{\mathbf{y}_{\phi,i}\}_{i=1}^{T}$, which eliminates the unobservability issue for the projected carrier phase measurements. Thus, $\{\mathbf{y}_{\phi,i}\}_{i=1}^{T}$ can now be projected from $\mathbb{R}^{M}$ to $\mathbb{R}^{\tilde{M}}$ for the second-stage FGO. Analogous to (20), the optimal measurement projection for $\mathbf{y}_{\phi,i}$ can be formulated as

$$\boldsymbol{\Psi}_{\phi,i}^{*} = \underset{\boldsymbol{\Psi}_i}{\mathrm{argmin}}\, \mathrm{Tr}\left(\{(\boldsymbol{\Psi}_i\mathbf{H}_{\mathbf{p}_i})^{\top}(\boldsymbol{\Psi}_i\mathbf{R}_{\phi,i}\boldsymbol{\Psi}_i^{\top})^{-1}(\boldsymbol{\Psi}_i\mathbf{H}_{\mathbf{p}_i})\}^{-1}\right) \tag{22}$$

where $\mathbf{H}_{\mathbf{p}_i} = \left(\partial \mathbf{h}(\mathbf{p}_i)\right) / \left(\partial \mathbf{p}_i\right)|_{\mathbf{p}_i=\hat{\mathbf{p}}_i}$. Note that $\hat{\mathbf{p}}_i$ here is the position estimate computed from the first-stage FGO. Similarly, the error factor of the projected carrier phase is expressed by

$$\|\tilde{e}_{\phi,i}^{\mathrm{II}}\|_{\tilde{\mathbf{R}}_{\phi,i}}^{2} = \|\boldsymbol{\Psi}_{\phi,1}^{*}\mathbf{y}_{\phi,i} - \boldsymbol{\Psi}_{\phi,1}^{*}\mathbf{h}(\mathbf{x}_i) - \lambda\boldsymbol{\Psi}_{\phi,1}^{*}\hat{\mathbf{n}}_{\mathrm{i,fix}}\|_{\tilde{\mathbf{R}}_{\phi,i}}^{2} \tag{23}$$

where $\tilde{\mathbf{R}}_{\phi,i} = \boldsymbol{\Psi}_{\phi,1}^{*}\mathbf{R}_{\phi,i}\boldsymbol{\Psi}_{\phi,1}^{*\top}$. Accordingly, the objective functions of the first and second-stage FGOs can be written as (24) and (25) respectively. The measurement projection scheme is summarized in Algorithm 1.

$$\begin{aligned}
\hat{\mathbf{x}}_{1:\mathrm{T,float}}, \hat{\mathbf{n}}_{1:\mathrm{T,float}} = \underset{\mathbf{x}_{1:\mathrm{T}}, \mathbf{n}_{1:\mathrm{T}}}{\mathrm{argmin}} \|e_{\mathrm{pri}}^{\mathrm{I}}\|_{\mathbf{P}_{\mathrm{pri}}}^{2} + \textstyle\sum_{i=1}^{T}(\|e_{\phi,i}^{\mathrm{I}}\|_{\tilde{\mathbf{R}}_{\phi,i}}^{2} + \\
\|\tilde{e}_{\rho,i}\|_{\tilde{\mathbf{R}}_{\rho,i}}^{2}) + \textstyle\sum_{i=1}^{T-1}(\|e_{x,i}\|_{\tilde{\mathbf{Q}}_i}^{2} + \|e_{n,i}\|_{\mathbf{V}_i}^{2}).
\end{aligned} \tag{24}$$

$$\begin{aligned}
\hat{\mathbf{x}}_{1:\mathrm{T,fix}} = \underset{\mathbf{x}_{1:\mathrm{T}}}{\mathrm{argmin}} \|e_{\mathrm{pri}}^{\mathrm{II}}\|_{\mathbf{P}_{1,\mathrm{float}}}^{2} + \textstyle\sum_{i=1}^{T}(\|\tilde{e}_{\phi,i}^{\mathrm{II}}\|_{\tilde{\mathbf{R}}_{\phi,i}}^{2} + \|\tilde{e}_{\rho,i}\|_{\tilde{\mathbf{R}}_{\rho,i}}^{2}) \\
+ \textstyle\sum_{i=1}^{T-1} \|e_{x,i}\|_{\tilde{\mathbf{Q}}_i}^{2}.
\end{aligned} \tag{25}$$

VI. Measurement Projection Scheme II

As shown in the middle diagram of Fig. 1, the first-stage FGO uses the original carrier phase measurements $\{\mathbf{y}_{\phi,i}\}_{i=1}^{T} \in \mathbb{R}^{M}$. Thus, despite projecting the pseudorange measurements to the subspace $\mathbb{R}^{\tilde{M}}$, the first FGO's dimensionality remains $(6+M)\times T$. To further reduce computational cost, it is desirable to also project the carrier phase measurements. Measurement projection scheme II achieves this by projecting carrier phase measurements into a lower-dimensional subspace while preserving observability of the integer ambiguities. The algorithm of the projection scheme II is illustrated in the right diagram in Fig. 1.

For carrier phase measurement $\mathbf{y}_{\phi,i} \in \mathbb{R}^{M}$ and a linear projection matrix $\boldsymbol{\Psi}_{\phi,i} \in \mathbb{R}^{\tilde{M}\times M}$ $(\tilde{M} < M)$, the projected carrier phase can be expressed as

$$\tilde{\mathbf{y}}_{\phi,i} = \boldsymbol{\Psi}_{\phi,i}\mathbf{h}(\mathbf{x}_i) + \lambda\boldsymbol{\Psi}_{\phi,i}\mathbf{n}_i + \boldsymbol{\Psi}_{\phi,i}\boldsymbol{\eta}_i \tag{26}$$

where $\mathbf{n}_i \in \mathbb{Z}^{M}$ and $\tilde{\mathbf{y}}_{\phi,i} \in \mathbb{R}^{\tilde{M}}$. However, using the projected $\tilde{\mathbf{y}}_{\phi,i}$ in the FGO renders the ambiguity $\mathbf{n}_i$ unobservable. To address this, we define the projected ambiguity $\mathbf{n}_i' = \boldsymbol{\Psi}_{\phi,i}\mathbf{n}_i \in \mathbb{R}^{\tilde{M}}$, which becomes fully observable given

Algorithm 1 Measurement Projection Scheme I

Define total time length L, sliding window size T
Set initial state estimate $\hat{\mathbf{x}}_0, \hat{\mathbf{n}}_0$ and covariance $\mathbf{P}_0$
Initialize $\mathbf{\Psi}_{\phi,0,[0]}, \mathbf{\Psi}_{\rho,0,[0]} \sim \mathcal{U}([-1,1]^{\tilde{M}\times M})$
Update $\mathbf{\Psi}_{\rho,0,[s]}$ using (18) for iterations $s:0\rightarrow N_\rho$
Update $\mathbf{\Psi}_{\phi,0,[s]}$ using (18) for iterations $s:0\rightarrow N_\phi$
for $k=1,...,L$ **do**
  Receive: $t_k, \mathbf{y}_k$
  if $k \le T$ **then**
    Update $\mathbf{\Psi}_{\rho,0,[s]}$ by (18) for $s:0\rightarrow N_\rho$ if $k>1$
    $\{\hat{\mathbf{x}}\}_{i=0,\text{float}}^{k}, \{\hat{\mathbf{n}}\}_{i=0,\text{float}}^{k} \leftarrow$ solve 1st FGO (24)
    $\{\hat{\mathbf{n}}\}_{i=0,\text{fix}}^{k} \leftarrow$ integer fixation
    Update $\mathbf{\Psi}_{\phi,0,[0]}$ by (18) for $s:0\rightarrow N_\phi$ if $k>1$
    $\{\hat{\mathbf{x}}\}_{i=0,\text{fix}}^{k} \leftarrow$ solve 2nd FGO (25)
    Set $\mathbf{\Psi}_{\rho,0,[0]}=\mathbf{\Psi}_{\rho,0,[N_\rho]}$, $\mathbf{\Psi}_{\phi,0,[0]}=\mathbf{\Psi}_{\phi,0,[N_\phi]}$
  else
    Set index $j=k-T+1$
    Set $\mathbf{\Psi}_{\rho,j,[0]} = \mathbf{\Psi}_{\rho,j-1,[N_\rho]}$, $\mathbf{\Psi}_{\phi,j,[0]} = \mathbf{\Psi}_{\phi,j-1,[N_\phi]}$
    Update $\mathbf{\Psi}_{\rho,j,[s]}$ using (18) for $s:0\rightarrow N_\rho$
    $\{\hat{\mathbf{x}}\}_{i=j,\text{float}}^{k}, \{\hat{\mathbf{n}}\}_{i=j,\text{float}}^{k} \leftarrow$ solve 1st FGO (24)
    $\{\hat{\mathbf{n}}\}_{i=j,\text{fix}}^{k} \leftarrow$ integer fixation
    Update $\mathbf{\Psi}_{\phi,j,[s]}$ using (18) for $s:0\rightarrow N_\phi$
    $\{\hat{\mathbf{x}}\}_{i=j,\text{fix}}^{k} \leftarrow$ solve 2nd FGO (25)
  end if
  Output $\hat{\mathbf{x}}_{k,\text{fix}}, \hat{\mathbf{n}}_{k,\text{fix}}$
end for

$\tilde{\mathbf{y}}_{\rho,i}$ and $\tilde{\mathbf{y}}_{\phi,i}$. This allows the first-stage FGO to operate in reduced dimensionality $(6+\tilde{M})*T$ by estimating $\mathbf{x}_i \in \mathbb{R}^6$ and $\mathbf{n}'_i \in \mathbb{R}^{\tilde{M}}$, thus lowering computational cost. However, $\mathbf{n}'_i$ loses its integer-valued property, making ambiguity resolution infeasible and degrading positioning accuracy [9]. To address this issue, we impose integer constraints on the projection operator $\mathbf{\Psi}_{\phi,i} \in \mathbb{Z}^{\tilde{M}\times M}$ such that $\mathbf{n}'_i$ remains integer-valued.

Equation (26) can be rewritten as

$$\tilde{\mathbf{y}}_{\phi,i} = \mathbf{\Psi}_{\phi,i}\mathbf{h}(\mathbf{x}_i) + \lambda\mathbf{n}'_i + \mathbf{\Psi}_{\phi,i}\boldsymbol{\eta}_i \tag{27}$$

To find the optimal integer-valued projection matrix $\mathbf{\Psi}_{\phi,i}$, an optimization program analogous to (15) is formulated. Since integer ambiguity resolution is crucial for GNSS-RTK positioning accuracy, the optimality criterion of the carrier phase projection is selected to minimize the MSE of the projected ambiguity estimate $\hat{\mathbf{n}}'$. The FIM $\boldsymbol{\mathcal{I}}(\mathbf{n}'_i)$ and the optimization problem can be formulated as follows.

$$\boldsymbol{\mathcal{I}}(\mathbf{n}'_i) = \mathbf{H}_{\mathbf{n}'_i}^\top(\mathbf{\Psi}_{\phi,i}\mathbf{R}_{\phi,i}\mathbf{\Psi}_{\phi,i}^\top)^{-1}\mathbf{H}_{\mathbf{n}'_i} = \lambda^2(\mathbf{\Psi}_{\phi,i}\mathbf{R}_{\phi,i}\mathbf{\Psi}_{\phi,i}^\top)^{-1} \tag{28}$$

$$\begin{aligned}\mathbf{\Psi}^*_{\phi,i} &= \underset{\mathbf{\Psi}_{\phi,i}\in\mathbb{Z}^{\tilde{M}\times M}}{\operatorname{argmin}} \operatorname{Tr}\left(\{\boldsymbol{\mathcal{I}}^{-1}(\mathbf{n}'_i)\}\right)\\ &= \underset{\mathbf{\Psi}_{\phi,i}\in\mathbb{Z}^{\tilde{M}\times M}}{\operatorname{argmin}} \frac{1}{\lambda^2}\sum_{k=1}^{\tilde{M}} \mathbf{\Psi}_{\phi,i}(k,:)\mathbf{R}_{\phi,i}\mathbf{\Psi}_{\phi,i}^\top(k,:)\end{aligned} \tag{29}$$

where $\mathbf{H}_{\mathbf{n}'_i} = (\partial\tilde{\mathbf{y}}_{\phi,i}) / (\partial\mathbf{n}'_i)\,|_{\mathbf{n}'_i=\hat{\mathbf{n}}'_i} = \lambda\mathbf{I}_{\tilde{M}\times\tilde{M}}$, due to the linear structure of $\mathbf{n}'_i$ in $\tilde{\mathbf{y}}_{\phi,i}$. $\mathbf{\Psi}_{\phi,i}(k,:)$ is the k-th row of $\mathbf{\Psi}_{\phi,i}$. $\mathbf{R}_{\phi,i}$ is the noise covariance matrix of DD carrier phase measurements, which can be derived as follows. Denote the differencing operator by $\boldsymbol{\mathcal{S}} \in \mathbb{Z}^{M\times(M+1)}$ and the noise covariance matrix of SD carrier phase measurements by $\mathbf{R}^{\text{SD}}_{\phi,i} \in \mathbb{R}^{(M+1)\times(M+1)}$.

$$\boldsymbol{\mathcal{S}} = \begin{bmatrix}\mathbf{1}_{\text{M}\times 1} & -\mathbf{I}_{\text{M}\times\text{M}}\end{bmatrix}, \mathbf{R}^{\text{SD}}_{\phi,i} = \operatorname{diag}\left(\sigma^2_{\phi_1}\ \sigma^2_{\phi_2}\ \cdots \sigma^2_{\phi_{\text{M+1}}}\right) \tag{30}$$

And $\mathbf{R}_{\phi,i}$ can be computed by $\mathbf{R}_{\phi,i} = \boldsymbol{\mathcal{S}}\mathbf{R}^{\text{SD}}_{\phi,i}\boldsymbol{\mathcal{S}}^\top$ as follows.

$$\mathbf{R}_{\phi,i} = \begin{bmatrix}\sigma^2_{\phi_1}+\sigma^2_{\phi_2} & \sigma^2_{\phi_1} & \cdots & \sigma^2_{\phi_1}\\ \sigma^2_{\phi_1} & \sigma^2_{\phi_1}+\sigma^2_{\phi_3} & \cdots & \sigma^2_{\phi_1}\\ \vdots & \vdots & \vdots & \vdots\\ \sigma^2_{\phi_1} & \sigma^2_{\phi_1} & \cdots & \sigma^2_{\phi_1}+\sigma^2_{\phi_{\text{M+1}}}\end{bmatrix} \tag{31}$$

As indicated by (28), $\operatorname{rank}(\mathbf{\Psi}_{\phi,i}) = \tilde{M}$ is required to ensure the matrix inverse exits, adding a rank constraint to the optimization in (29). The optimal $\mathbf{\Psi}^*_{\phi,i}$ of (29) can be determined as follows: For the k-th row $\mathbf{\Psi}_{\phi,i}(k,:)$, find the index of the k-th smallest diagonal entry of $\mathbf{R}_{\phi,i}$, set the corresponding entry of $\mathbf{\Psi}_{\phi,i}(k,:)$ to 1 and all others to zero. For instance, for the first row vector $\mathbf{\Psi}_{\phi,i}(1,:)$, if $\mathbf{R}_{\phi,i}(4,4)$ is the smallest among all diagonal entries, then set $\mathbf{\Psi}_{\phi,i}(1,4)=1$ and everywhere else to zero. Repeat this process for $k=1,2,3,\cdots,\tilde{M}$ until $\mathbf{\Psi}_{\phi,i}$ is populated. In this way, the integer-valued optimal projection operator $\mathbf{\Psi}^*_{\phi,i}$ can be determined to minimize the objective function in (29) while satisfying the rank constraint.

An observation about the optimal $\mathbf{\Psi}^*_{\phi,i}$ is that its $\tilde{M}$ non-zero entries correspond to a subset of the carrier phase measurement $\mathbf{y}_{\phi,i} \in \mathbb{R}^M$ with the smallest $\tilde{M}$ variances (the diagonal entries of $\mathbf{R}_{\phi,i}$). In effect, the projected $\tilde{\mathbf{y}}_{\phi,i} \in \mathbb{R}^{\tilde{M}}$ is formed by selecting from $\mathbf{y}_{\phi,i}$ the entries with the smallest $\tilde{M}$ variances. Thus, the optimal projection for $\mathbf{y}_{\phi,i}$ is effectively an optimal measurement selection problem. However, unlike projection scheme I, where all measurements are used, projection scheme II uses only a subset of the original carrier phase measurements. Therefore, a slight performance degradation is expected in projection scheme II compared to scheme I.

Assume $\mathbf{R}_{\phi,i}$ remains approximately constant within the sliding window, $\mathbf{\Psi}^*_{\phi,1}$ computed at the first time step within the sliding window can be reused to project $\{\mathbf{y}_{\phi,i}\}_{i=1}^T$ for the entire window. Thus, the error factor of the projected carrier phase in the first-stage FGO can be expressed by

$$\|\tilde{e}^{\text{I}}_{\phi,i}\|^2_{\tilde{\mathbf{R}}_{\phi,i}} = \|\mathbf{\Psi}^*_{\phi,1}\mathbf{y}_{\phi,i} - \mathbf{\Psi}^*_{\phi,1}\mathbf{h}(\mathbf{x}_i) - \lambda\mathbf{n}'_i\|^2_{\tilde{\mathbf{R}}_{\phi,i}} \tag{32}$$

where $\tilde{\mathbf{R}}_{\phi,i} = \mathbf{\Psi}^*_{\phi,1}\mathbf{R}_{\phi,i}\mathbf{\Psi}^{*\top}_{\phi,1}$. Since the first-stage FGO also estimates the projected ambiguity $\mathbf{n}'$ in projection scheme II, the adaptive ambiguity factor must be modified as follows.

$$\|e_{\mathbf{n}',i}\|^2_{\tilde{\mathbf{V}}_i} = \|\mathbf{n}'_{i+1} - \mathbf{n}'_i\|^2_{\tilde{\mathbf{V}}_i}. \tag{33}$$

where $\tilde{\mathbf{V}}_i = \mathbf{\Psi}^*_{\phi,1}\mathbf{V}_i\mathbf{\Psi}^{*\top}_{\phi,1}$. After the integer ambiguity resolution, the integer-valued projected ambiguity estimates

$\{\hat{\mathbf{n}}'_i\}_{i=1}^T$ are obtained. In the second-stage FGO, the error factor of the projected carrier phase is computed as

$$\|\tilde{e}^{\text{II}}_{\phi,i}\|^2_{\tilde{\mathbf{R}}_{\phi,i}} = \|\mathbf{\Psi}^*_{\phi,1}\mathbf{y}_{\phi,i} - \mathbf{\Psi}^*_{\phi,1}\mathbf{h}(\mathbf{x}_i) - \lambda\hat{\mathbf{n}}'_i\|^2_{\tilde{\mathbf{R}}_{\phi,i}} \quad (34)$$

The projection for pseudorange measurements in projection scheme II is identical to that in projection scheme I and is not repeated here for brevity. Using (10), (12), (21), (32), (33) and (34), the objective functions for the first and second-stage FGOs of projection scheme II are formulated. The overall procedure is summarized in Algorithm 2.

$$\hat{\mathbf{x}}_{1:\text{T,float}}, \hat{\mathbf{n}}'_{1:\text{T,float}} = \underset{\mathbf{x}_{1:\text{T}}, \mathbf{n}'_{1:\text{T}}}{\operatorname{argmin}} \|e^{\text{I}}_{\text{pri}}\|^2_{\mathbf{P}_{\text{pri}}} + \textstyle\sum_{i=1}^T (\|\tilde{e}^{\text{I}}_{\phi,i}\|^2_{\tilde{\mathbf{R}}_{\phi,i}} + \|\tilde{e}_{\rho,i}\|^2_{\tilde{\mathbf{R}}_{\rho,i}}) + \textstyle\sum_{i=1}^{T-1} (\|e_{x,i}\|^2_{\tilde{\mathbf{Q}}_i} + \|e_{\mathbf{n}',i}\|^2_{\tilde{\mathbf{V}}_i}). \quad (35)$$

$$\hat{\mathbf{x}}_{1:\text{T,fix}} = \underset{\mathbf{x}_{1:\text{T}}}{\operatorname{argmin}} \|e^{\text{II}}_{\text{pri}}\|^2_{\mathbf{P}_{1,\text{float}}} + \textstyle\sum_{i=1}^T (\|\tilde{e}^{\text{II}}_{\phi,i}\|^2_{\tilde{\mathbf{R}}_{\phi,i}} + \|\tilde{e}_{\rho,i}\|^2_{\tilde{\mathbf{R}}_{\rho,i}}) + \textstyle\sum_{i=1}^{T-1} \|e_{x,i}\|^2_{\tilde{\mathbf{Q}}_i}. \quad (36)$$

Algorithm 2 Measurement Projection Scheme II

1: Define total time length L, sliding window size T
2: Set initial state estimate $\hat{\mathbf{x}}_0, \hat{\mathbf{n}}_0$ and covariance $\mathbf{P}_0$
3: Initialize $\mathbf{\Psi}_{\rho,0} \sim \mathcal{U}([-1,1]^{\tilde{M}\times M})$
4: Update $\mathbf{\Psi}_{\rho,0,[s]}$ using (18) for iterations $s: 0 \to N_\rho$
5: **for** $k = 1, ..., L$ **do**
6: **Receive:** $t_k, \mathbf{y}_k$
7: **if** $k \leq T$ **then**
8: Update $\mathbf{\Psi}_{\rho,0,[s]}$ by (18) for $s: 0 \to N_\rho$ if $k > 1$
9: Obtain $\mathbf{\Psi}_{\phi,0}$ by solving (29)
10: $\{\hat{\mathbf{x}}\}^k_{i=0,\text{float}}, \{\hat{\mathbf{n}}'\}^k_{i=0,\text{float}} \leftarrow$ solve 1st FGO (35)
11: $\{\hat{\mathbf{n}}'\}^k_{i=0,\text{fix}} \leftarrow$ integer fixation
12: $\{\hat{\mathbf{x}}\}^k_{i=0,\text{fix}} \leftarrow$ solve 2nd FGO (36)
13: Set $\mathbf{\Psi}_{\rho,0,[0]} = \mathbf{\Psi}_{\rho,0,[N_\rho]}$
14: **else**
15: Set index $j = k - T + 1$
16: Set $\mathbf{\Psi}_{\rho,j,[0]} = \mathbf{\Psi}_{\rho,j-1,[N_\rho]}$
17: Update $\mathbf{\Psi}_{\rho,j,[s]}$ using (18) for $s: 0 \to N_\rho$
18: Obtain $\mathbf{\Psi}_{\phi,j}$ by solving (29)
19: $\{\hat{\mathbf{x}}\}^k_{i=j,\text{float}}, \{\hat{\mathbf{n}}'\}^k_{i=j,\text{float}} \leftarrow$ solve 1st FGO (35)
20: $\{\hat{\mathbf{n}}'\}^k_{i=j,\text{fix}} \leftarrow$ integer fixation
21: $\{\hat{\mathbf{x}}\}^k_{i=j,\text{fix}} \leftarrow$ solve 2nd FGO (36)
22: **end if**
23: Output $\hat{\mathbf{x}}_{k,\text{fix}}, \hat{\mathbf{n}}'_{k,\text{fix}}$
24: **end for**

VII. Numerical Simulation

A. Simulation Setup

A numerical simulation is conducted to demonstrate the proposed measurement projection schemes. The following approaches are compared: (1) The baseline FGO-based GNSS-RTK positioning algorithm (denoted by FGO-BASE); (2) The baseline FGO-based GNSS-RTK with optimal measurement projection scheme I (denoted by FGO-MP-I); (3) The baseline FGO-based GNSS-RTK with optimal measurement projection scheme II (denoted by FGO-MP-II);

The simulation considers a single-band GNSS receiver collecting pseudorange and carrier phase signals from $M + 1 = 13$ satellites at a sampling rate of 10 Hz. The carrier wavelength is $\lambda = 0.2$ m. A static base station with a known position is located in close proximity to the receiver. At each epoch, $M = 12$ double-differenced pseudorange and carrier phase measurements are available. To simulate the frequent cycle slips common in dynamic environments, such as urban canyons, multiple integer jumps are introduced in the time evolution of integer ambiguities in the carrier phase measurements, using the method described in [6]. Receiver motion follows the CV model in (6) with a sampling interval of $dt = 0.1$ s. Each simulation lasts 300 time steps.

The baseline algorithm FGO-BASE processes GNSS measurements in full dimensionality. In FGO-MP-I, both pseudorange and carrier phase measurements are projected to the subspace of dimensionality $\tilde{M} = 3$. In FGO-MP-II, pseudorange is projected to $\tilde{M} = 3$ and carrier phase to $\tilde{M} = 6$. For projection optimization, single gradient descent iteration is used at lines $9, 12, 18, 21$ in Algorithm 1 and lines $8, 17$ in Algorithm 2, as warm-started optimization requires very few iterations per time step in our experience [3]. The number of gradient descent iterations can be tuned based on the trade-off between computational cost and MSE performance. All algorithms are implemented in Matlab, using CasADi [1] via the MPCTools [10] interface and Ipopt [13] to solve the FGO on a laptop with an i7 2.6GHz CPU.

B. Performance Evaluation

Fig. 2 compares the integer ambiguity resolution of FGO-MP-I and FGO-MP-II with the true ambiguity history in a single simulation test, using a sliding window of size $T = 90$. FGO-MP-I estimates the original ambiguities, while FGO-MP-II estimates the projected ambiguities. Both algorithms demonstrate effective ambiguity fixation. Although relatively larger errors appear during the initial transient phase, the ambiguity estimates quickly converge to the true values. Fig. 3 shows the receiver state estimation errors for all three algorithms. These errors are of the same order of magnitude and are very close to each other, indicating that the proposed projection schemes maintain positioning accuracy comparable to the baseline approach. However, further performance evaluation via Monte Carlo simulations is necessary for statistical validation.

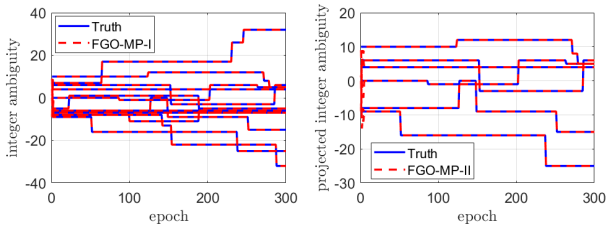

Fig. 2. Integer ambiguity resolution of FGO-MP-I (left) and FGO-MP-II(right)

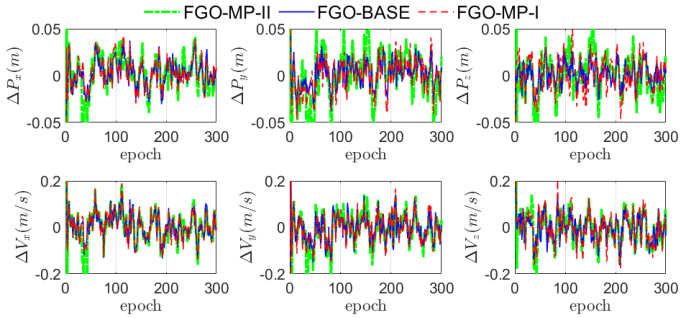

Fig. 3. Receiver states estimation errors

C. Monte Carlo Simulation Results

A Monte Carlo (MC) simulation study with 100 runs–each initialized randomly–is conducted to statistically evaluate the proposed algorithms. The root-mean-square errors (RMSE) of the receiver position estimates for the three algorithms, using a sliding window size of $T = 90$, are shown in Fig. 4. After the initial transient phase, all three RMSE curves converge to below 5 cm. Both FGO-MP-I (red) and FGO-MP-II (green) closely track the baseline RMSE of the FGO-BASE, demonstrating that the proposed projection schemes can maintain high-precision positioning accuracy while offering the potential benefits of reducing computational complexity. A closer look at the post-transient RMSE (after 90 epochs) shows that FGO-BASE achieves the smallest RMSE, followed by FGO-MP-I, with FGO-MP-II exhibiting the largest RMSE level. This aligns with our analysis that (1) the baseline FGO-BASE processes full-dimensional measurements, thus achieving the highest accuracy; (2) FGO-MP-II exhibits the largest RMSE as it sacrifices some accuracy by selecting only a subset of the carrier phase data. Additional MC simulations with sliding window sizes $T = 30$, 50, 70, and 110 showed consistent results. However, these additional results are not reported here due to space limitations.

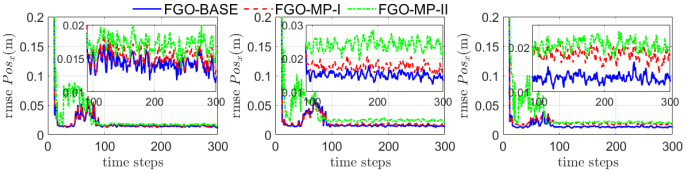

Fig. 4. Root-mean-square-errors (RMSE) of the receiver position estimates for the three algorithms with sliding window size $T = 90$ and 100 MC runs.

In addition to positioning accuracy, the computational complexity of the three algorithms is assessed for varying sliding window sizes. Fig. 5 shows the average runtime of the algorithms for different window sizes, computed over 100 MC runs, in an unoptimized Matlab implementation. As expected, runtime increases with the sliding window size for all algorithms. Both proposed measurement projection algorithms, FGO-MP-I and FGO-MP-II, consistently achieve lower runtime than the baseline FGO-BASE. Moreover, FGO-MP-II outperforms FGO-NP-I in runtime, as it further reduces the computational load by projecting the carrier phase measurements in the first-stage FGO.

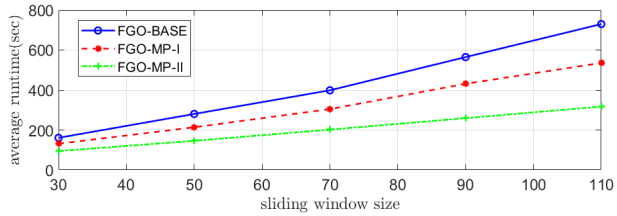

Fig. 5. Average runtime of the three algorithms with different sliding window sizes in Matlab implementation. 100 MC runs for each sliding window size.

VIII. Conclusion

This paper proposes two optimal measurement projection schemes to reduce the computational complexity of factor-graph-based GNSS-RTK positioning. By projecting GNSS measurements into lower-dimensional subspaces, the approach accelerates optimization while maintaining high-precision positioning with minimal accuracy loss. Monte Carlo simulations validate its efficiency, demonstrating its potential to improve the computational efficiency of FGO-based GNSS-RTK, especially in computationally constrained environments. Future work will apply the proposed methods to iSAM/iSAM2 for further computational efficiency gains.

References

[1] J.A.E. Andersson and et al. CasADi – A software framework for nonlinear optimization and optimal control. *Math. Program. Comput.*, 11(1):1–36, 2019.

[2] J. Farrell. *Aided navigation: GPS with high rate sensors*. McGraw-Hill, Inc., 2008.

[3] M. Greiff and K. Berntorp. Optimal measurement projections with adaptive mixture kalman filtering for gnss positioning. In *2020 ACC*, pages 4435–4441. IEEE, 2020.

[4] F. Gustafsson. *Statistical sensor fusion*. Studentlitteratur, 2010.

[5] W. Hu, Y. Hu, M. Stas, and J. Farrell. Optimization-based outlier accommodation for tightly coupled rtk-aided inertial navigation systems in urban environments. *arXiv preprint arXiv:2407.13912*, 2024.

[6] Y. Hu, S. Di Cairano, and K. Berntorp. GNSS-RTK Factor Graph Optimization with Adaptive Ambiguity Noise. *accepted to the 2025 ACC*, 2025.

[7] M. Kaess and et al. isam2: Incremental smoothing and mapping using the bayes tree. *The Int. J. Robot. Res.*, 31(2):216–235, 2012.

[8] M. Kaess, A. Ranganathan, and F. Dellaert. isam: Incremental smoothing and mapping. *IEEE Trans. Robot.*, 24(6):1365–1378, 2008.

[9] S. M. Kay. *Fundamentals of Statistical Signal Processing: Estimation Theory*. Prentice Hall, 1993.

[10] M. Risbeck and J. B. Rawlings. MPCTools: Nonlinear model predictive control tools for CasADi (Octave interface). `https://bitbucket.org/rawlings-group/octave-mpctools`, 2016.

[11] T. Suzuki. Time-relative rtk-gnss: Gnss loop closure in pose graph optimization. *IEEE Robot. Autom. Lett.*, 5(3):4735–4742, 2020.

[12] P.J.G. Teunissen, P.J. De Jonge, and CCJM Tiberius. Performance of the lambda method for fast gps ambiguity resolution. *Navig.*, 44(3):373–383, 1997.

[13] A. Wächter and L. T. Biegler. On the implementation of an interior-point filter line-search algorithm for large-scale nonlinear programming. *Math. Program.*, 106:25–57, 2006.

[14] W. Wen and L-T Hsu. Towards robust gnss positioning and real-time kinematic using factor graph optimization. In *2021 IEEE ICRA*, pages 5884–5890. IEEE, 2021.

[15] S. Zhao, Y. Chen, and J. Farrell. High-precision vehicle navigation in urban environments using an mem's imu and single-frequency gps receiver. *IEEE Trans. Intel. Transp. Syst.*, 17(10):2854–2867, 2016.